PHYSICAL REVIEW A **100**, 053405 (2019)

Electron correlation in channel-resolved strong-field molecular double ionization

Chuan Cheng,[1] Patricia Vindel-Zandbergen,[2] Spiridoula Matsika,[2] and Thomas Weinacht[1]
[1]*Department of Physics, Stony Brook University, Stony Brook, New York 11794, USA*
[2]*Department of Chemistry, Temple University, Philadelphia, Pennsylvania 19122, USA*

(Received 3 July 2019; revised manuscript received 24 August 2019; published 8 November 2019)

Strong-field ionization plays a fundamental role in attosecond science as the source of electron wave packets which ultimately provide attosecond bursts of radiation as they are driven back to the atom or molecule of origin. Double ionization is an important probe of electron correlation (correlated electron dynamics), which lies at the core of attosecond science. While double ionization of atoms has been studied extensively, the double ionization of molecules is relatively unexplored—particularly for the case of polyatomic systems. We present coincidence (three and four particle) velocity map imaging measurements of molecular double ionization in 1,3-cyclohexadiene and 1,4-cyclohexadiene using few cycle (∼10 fs) laser pulses. Our measurements allow us to distinguish between dissociative and nondissociative double ionization, and we find a difference in the correlation of electrons that come from the different channels.

DOI: 10.1103/PhysRevA.100.053405

I. INTRODUCTION

The interaction of atoms and molecules with intense ultrafast laser pulses is interesting from at least two perspectives. One is the intrinsic strong-field dynamics that take place during the light-matter interaction, and the other is the access to even shorter timescales given the highly nonlinear response of the driven electrons to the applied field [1–3]. Studies of strong-field atomic and molecular ionization have led to new light sources and molecular imaging techniques, such as high harmonic generation (HHG) [4–8], laser induced electron diffraction (LIED) [9–11], and Coulomb explosion imaging (CEI) [12–15]. The first two rely explicitly on recollision physics, where an electron which is initially removed by the strong laser field can be driven back to the ionic core and scatter (elastically or inelastically), providing soft x-ray radiation (HHG), information on (time-dependent) molecular structure (LIED), or drive further nonsequential double ionization (NSDI).

NSDI is one of the most fundamental and important phenomena in strong-field physics, and has attracted interest as a probe of electron correlation and the physics of inelastic rescattering (see Ref. [16] and references therein). Following the first measurements in Xe atoms [17], there have been many experimental and theoretical efforts, focusing mainly on atomic systems [18–23] and small molecules [24–27]. While there can in principle be many different mechanisms underlying NSDI (such as "shake-off" [19,28] or collective tunneling [29]), rescattering has been accepted to be the dominant one [4,30,31].

Following tunnel ionization, the first electron is accelerated by the laser field and driven back to the ion core.[1] If the energy of the recolliding electron is sufficiently high (e.g., greater than the second ionization potential), it can "knock out" a second electron directly in an inelastic collision [recollision impact ionization (RII)] [32–38]. If the return energy of the first electron is less than the second ionization potential, then it cannot knock out a second electron from the molecule. Instead, the energy transferred to the core can be enough to excite the electron to an excited bound state of the molecular cation, from which it can subsequently tunnel ionize in the laser field. This mechanism is known as recollision-induced excitation with subsequent tunnel ionization (RESI) [39–45]. A third possibility is that the returning electron is recaptured and forms a transient doubly excited state, from which the two electrons are subsequently removed by the laser field [46–48].

Different double ionization (DI) mechanisms lead to different final momentum distributions and correlations for the two electrons. RESI is typically associated with cross shaped patterns in the correlation plots for the electron momenta along the laser polarization axis [44,49–54]. In contrast, RII can lead to both correlations and anticorrelations between the momenta for the two electrons along the laser polarization axis, leading to features along the diagonal (quadrants 1 and 3) or antidiagonal (quadrants 2 and 4). These correlations have been found to depend on the laser intensity and pulse duration [44,55].

The rescattering dynamics can depend not only on the intensity of the laser field and the energy of the returning electron, but also on the structure of the molecule from which the electron is removed and with which it recollides. It has been shown that the correlated electron-momentum distribution in NSDI of diatomic molecules depends on the ground-state orbital symmetries and alignment with respect to the laser polarization axis [39,43,56,57]. Furthermore, different ionization pathways may show up in the DI yield and in the correlated electron momentum distribution [58–61] which can

---

[1] We note that the initial ionization that takes place in our experiments has mixed "tunnel" and "multiphoton" character, given that the Keldysh parameter is only slightly lower than 1 (0.85), and there can be some resonant enhancement of the ionization yield from intermediate neutral states.

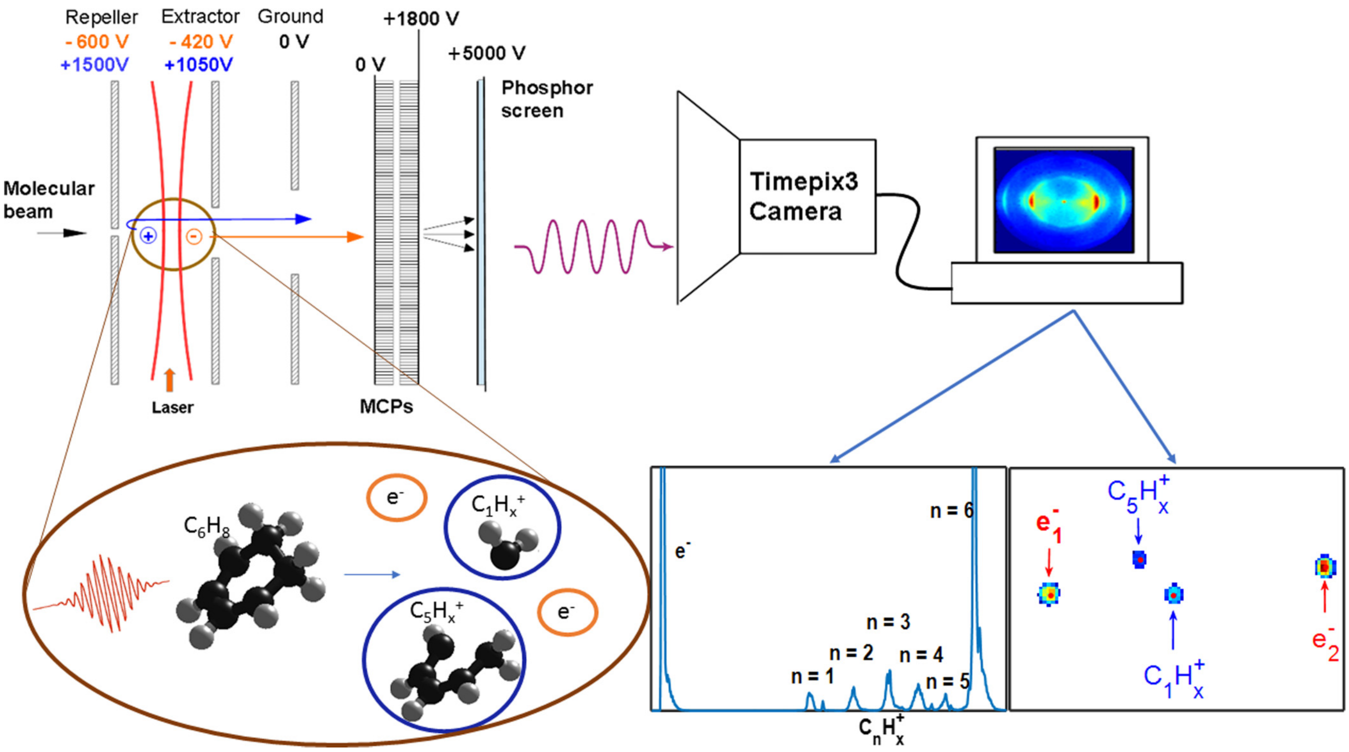

FIG. 1. Experimental apparatus for measuring electron-electron correlation spectrum in coincidence with specific ion fragmentation channels. The ion channel here is the $C_1H_X{}^+ + C_5H_X{}^+$ pair from 1,3-CHD. The top panel shows a schematic diagram of the apparatus. The bottom left panel illustrates the "reactants" (neutral molecule and intense laser pulse) and "products" (electrons and fragment ions). The bottom right panels show the time of flight mass spectrum as well as the hits from a quadruple coincidence double ionization event.

be related to the electronic structure of the molecules. Here we study molecular DI of 1,3-cyclohexadiene (1,3-CHD) and 1,4-cyclohexadiene (1,4-CHD) with coincidence velocity map imaging using a high speed time stamping camera. We separate electrons from different DI channels corresponding to different final states of the molecular dication. As with earlier work on benzene (C_6H_6) [62], we compare measurements for electrons coming from dissociative DI with electrons coming from nondissociative DI. We find a more pronounced difference in the correlation plots than was seen in earlier work. Our measurements and calculations suggest that RESI dominates the dissociative DI yield, while a mixture of RII and RESI occur for the case of nondisociative DI.

II. EXPERIMENTAL APPARATUS

Our measurements made use of an amplified Ti:sapphire system which produces 1 mJ laser pulses with a full width at half maximum (FWHM) duration of 30 fs and a central wavelength of 780 nm, at a repetition rate of 1 kHz. We make use of filamentation in Ar gas to broaden the spectral bandwidth by over a factor of 4 and an acousto-optic based pulse shaper to compress the pulses to under 10 fs duration (FWHM) [63,64]. These pulses are focused into an effusive beam of molecules by a 5 cm focal length curved mirror in our vacuum chamber, which is kept at a base pressure of about 10^{-10} Torr. An overall focal area of 500 μm^2 is estimated. The peak intensity of the laser pulses was between 60 and 100 TW/cm^2 for the coincidence measurements and 60 and 200 TW/cm^2 for the noncoincidence measurements. (See Fig. 1.)

Fragment ions and electrons are both collected in our coincidence velocity map imaging (VMI) apparatus, which makes use of a single detector and switching of the VMI lens voltages in order to first collect electrons and then ions after the polarity of the VMI voltage is switched. Since the time between ionization and detection of the electrons is small (less than 100 ns), we can neglect the motion of the ions before the voltage on the VMI plates is switched. We make use of a TIMEPIX3 time stamping camera [65,66], which has ~1 ns time resolution in order to separately measure the time of arrival and position of electrons and different fragment ions. For the ions, the timing serves as a measure of the longitudinal momentum, allowing us to measure the full three-dimensional momentum distribution without Abel inversion. For the electrons, the timing resolution is insufficient, and one would need to Abel invert the data in order to recover the full three-dimensional momentum. Here we focus on the momentum along the laser polarization axis, and therefore do not invert the data. For the triple (one ion and two electrons) and quadruple (two ions and two electrons) coincidence measurements described below, we make use of very low sample pressures (3×10^{-10} Torr) in order to keep the average number of ionized molecules per laser shot very low (~0.3).

Given the time resolution of our apparatus, if two electrons are produced with the same p_x and p_y, then this will lead to overlapping hits on the detector. The two electrons will be recorded as one. This leads to a systematic underrepresentation of electrons with the same *x* and *y* momentum (i.e., along the diagonals for the correlation plots shown below). However, despite this systematic error, we can still measure the momentum of electrons in coincidence, which is not possible with COLTRIMS using a wire grid detector [67].

III. CALCULATIONS

In order to interpret our measurements we performed electronic structure calculations. The geometries of both 1,3-CHD and 1,4-CHD neutral molecules were optimized using density functional theory with the B3LYP functional [68,69] and 6-31G(d) basis set available in GAUSSIAN-09 program package [70].

We performed equation of motion for ionization potentials coupled cluster theory with single and double excitations (EOM-IP-CCSD) [71–73] calculations in Q-Chem [74] at the geometry of the neutral species to obtain the vertical ionization energies and excited states of the mono- and the dications. These calculations showed that excited states are formed by exciting electrons from different occupied orbitals (HOMO, HOMO-n) to LUMO and LUMO + n and the core electrons were frozen. The EOM-IP-CCSD method cannot predict accurately the doubly excited states as it tends to overestimate excitation energies for states with dominant single excitation character. Therefore, singlet and triplet states of the dication were obtained by using second-order multiconfiguration quasidegenerate perturbation theory (MCQDPT2) [75,76] as implemented in the GAMESS software program [77,78] to consider the dynamic correlation effects. We employed a cc-pVDZ basis set [79] and the orbitals were obtained from a multiconfigurational self-consistent field (MCSCF) calculation with a complete active space denoted as (16,11), which includes 16 electrons in 11 orbitals to consider the excitations to LUMO and LUMO + 1. These calculations were also performed to obtain the electronic states of the monocations with an active space (17,13) of 17 electrons in 13 orbitals to include excitations to LUMO, LUMO + 1, LUMO + 2, and LUMO + 3. The molecular orbitals of the neutral species were calculated at the Hartree-Fock level using a cc-pVDZ basis set.

IV. EXPERIMENTAL RESULTS

Our measurements recorded the position (x and y) and timing (with 1 ns resolution) for each charged particle incident on the microchannel plate and phosphor detector using the Timepix camera. The camera provides x, y, and t information for each pixel which goes over a predetermined threshold. As each charged particle ("hit") leads to multiple pixels going above threshold (typically between 10 and 100), we calculate the centroid for each hit and estimate the precise time of arrival by fitting the distribution of pixels above threshold. For the electrons, this measurement represents the projection of the full vector momentum into the x-y plane (with the laser polarized along the x direction) since the time resolution of the camera is insufficient to determine the z component of the momentum. For the ions, however, the time resolution of the camera is typically a small fraction (between 1/10 and 1/100) of the spread in time of arrival for ions with a given mass to charge ratio, and thus we can directly recover the full vector momentum for the ions without the need for an inverse Abel transform. Fragment ions with different mass to charge ratios are separated by different times of flight (TOF) in our measurements. This difference in TOF is generally sufficient to resolve fragment ions with different numbers of carbon atoms, but not different numbers of hydrogen atoms. The most important exception to this is the case of $C_6H_X{}^{2+}$ and $C_3H_X{}^+$, which have the same mass to charge ratio and therefore arrive at the same time. A more detailed analysis of the momentum distributions for these ions is required to separate them.

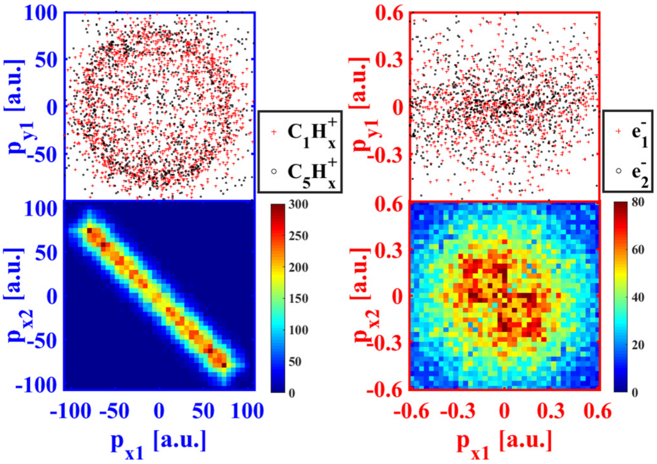

FIG. 2. Ion and electron images (top left and right panels, respectively) as well as correlation plots for ion and electron pairs (bottom left and right panels, respectively) measured in quadruple coincidence for 10 fs duration laser pulses with a peak intensity of about 40 TW/cm^2.The ion and electron images show a cross or circle for each particle detected, with only a small fraction of the total hits measured being displayed so that they can be seen clearly. The correlation plots show the number of ion and electron pairs arriving at our detector with the momentum along the laser polarization axis indicated by the x and y axes of the plots.

Figure 2 illustrates the basic quadruple coincidence results in the experiment. The top two panels show the raw hits for ions and electrons (top left and right panels, respectively). We note that only a fraction of the total hits are shown for clarity. The measurements shown here are for $C_1H_X{}^+$ (red cross) in coincidence with $C_5H_X{}^+$ (black circles). The bottom panels show the correlation between the momentum along the laser polarization axis for the two ions and the two electrons detected in each shot. As one can see from the bottom left panel, the x momenta of the fragment ions are almost perfectly anticorrelated with each other, consistent with the fact that they originate from the same parent molecule. The electrons display a more subtle anticorrelation, which is discussed in more detail below. In order to highlight the DI dynamics of interest, we look at correlations between electrons within specific momentum regions, measured in coincidence with ions within specific momentum regions, as illustrated in Fig. 3. In the left panel, which shows the distribution of $C_3H_X{}^+$ ions as a function of p_x and p_y, one can see both an inner (inside the inner dashed line) and outer ring of ions (between the dashed lines). The inner ring is mostly due to dissociative single

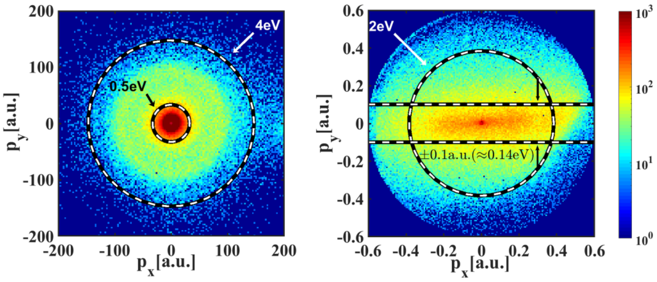

FIG. 3. Electron and ion images with regions of interest used when calculating electron correlations. The left panel shows a 2D ion momentum distribution for fragments arriving at the time of $C_3H_X{}^+$ (this includes both $C_3H_X{}^+$ as well as the parent dication, $C_6H_8{}^{2+}$). The inner dashed ring separates high and low KER ions. The right panel shows the 2D electron momentum distribution for electrons measured in coincidence with the ions shown on the left. The horizontal dashed lines illustrate the region of interest for electrons returning with low impact parameter.

ionization (SI), while the outer ring is almost exclusively due to dissociative DI (except in the case of $C_3H_X{}^+$ and $C_6H_X{}^{2+}$, for which the outer ring represents dissociative DI and the inner ring has contributions from nondissociative DI, as well as some dissociative DI) [58]. Thus we focus on dissociative DI by considering electrons in coincidence with fragment ions between the two dotted circles in the left panel of Fig. 3, and nondissociative DI by considering electrons in coincidence with $C_6H_X{}^{2+}$ ions that come inside the inner dotted circle at the same time of flight as $C_3H_X{}^+$ fragment ions. We highlight DI driven by recolliding electrons that have near zero impact parameter ("head on") collisions in the plane of the detector, leading us to select electrons with $p_y \leqslant 0.1$ a.u. We note that, since we do not have access to the z component of the electron momentum, we consider all impact parameters along z.

Figure 4 shows correlation plots for the x component of the momentum for pairs of electrons coming from DI of both 1,3-CHD and 1,4-CHD in coincidence with $C_3H_X{}^+$ fragments (left panels) or $C_6H_X{}^{2+}$(right panels). All four of the correlation plots show a cross pattern, which is associated with the RESI mechanism. This is discussed in more detail below. Here we note that both molecules display the same difference in the correlation plots for dissociative and nondissociative DI: the nondissociative channel shows a prominent feature along the antidiagonal, whereas electrons coming from the dissociative channel do not. This channel dependent correlation indicates that there must be differences in the dynamics leading to the population of different states of the molecular dication. As discussed in the calculation section, the electrons from nondissociative DI are primarily coming from the HOMO orbital, whereas electrons coming from dissociative channels are removed from deeper bound orbitals. In order to test the sensitivity of the correlation measurements to the intensity of the laser, we performed correlation measurements over a range of laser intensities. Figure 5 shows the correlation plots for dissociative and nondissociative DI for three different intensities. We note that the correlation plots are not very intensity dependent—the differences between electron correlations at different intensities are smaller than the differences between electron correlations for the two different channels.

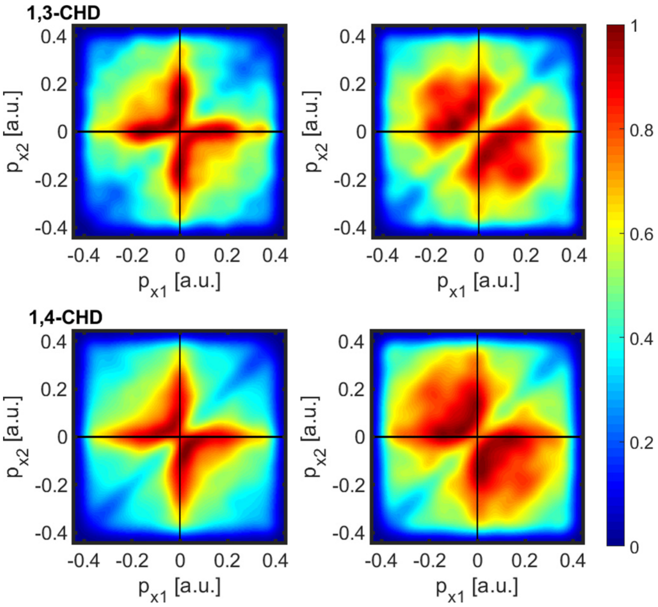

FIG. 4. Comparison of correlation plots (momentum parallel to the laser polarization axis) for electron pairs from dissociative and nondissociative channels of 1,3-CHD and 1,4-CHD. Left panels show the electron momentum correlation plots for the $C_3H_X{}^+$ dissociative channels of 1,3-CHD and 1,4-CHD, respectively. The right panels show the electron momentum correlation plots for the $C_6H_X{}^{2+}$ nondissociative channel. The measurements are for a peak intensity of 100 TW/cm^2. Black lines mark the positions of zero x momentum.

Figure 5 also shows the DI to SI ratio as a function of intensity. We note that the DI to SI ratio is much larger than predicted from a simple quasistatic tunnel ionization calculation (based on MO-ADK theory [80]). This highlights the fact that the DI is enhanced relative to the DI based on a quasistatic approximation, consistent with the idea that it is dominated by NSDI. Earlier measurements of nonsequential DI in atoms [81] also measured DI to SI ratios larger than predicted for sequential ionization, but significantly smaller than those

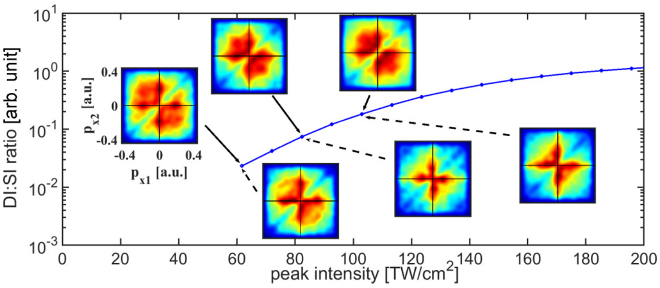

FIG. 5. Intensity dependence of DI for 1,3-CHD. The ratio between the DI and SI yields is plotted. The blue line is simply connecting the data points. Along the line, the comparison of electron correlations for dissociative and nondissociative channels is plotted. Correlation plots for nondissociative channels and dissociative channels are indicated with solid and dashed arrows, respectively. The yield of SI and DI channels are obtained by summing up all fragments from the inner and outer rings (inside the inner dashed line of Fig. 3, left panel, or between the two dashed lines), respectively [58].

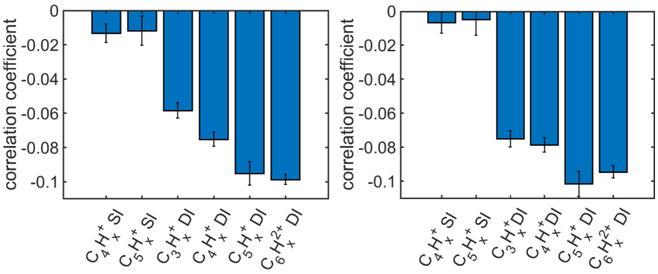

FIG. 6. Correlation coefficients for electron pairs measured in coincidence with different fragment ions. The left panel shows numbers calculated for 1,3-CHD ion channels. The right panel shows the same for 1,4-CHD. The measurements show that there is a nontrivial anticorrelation for electrons in coincidence with fragment ions having high KER as well as $C_6H_X{}^{2+}$ (all coming from DI). This is in contrast with the electrons measured in coincidence with low KER fragment ions (labeled with SI). The correlations are calculated for measurements with a laser intensity of 100 TW/cm^2. Error bars are obtained from a bootstrapping analysis.

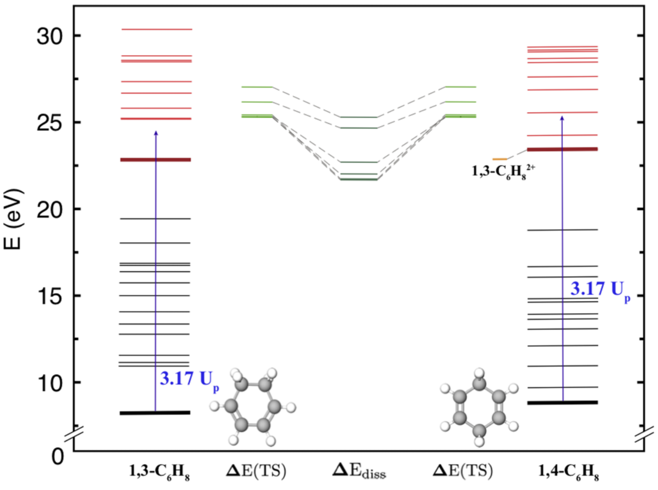

FIG. 7. Ground (thick lines) and excited states of the monocation (black lines) and the dication (red lines) for 1,3-CHD (left) and 1,4-CHD (right) calculated with the EOM-IP-CCSD method at the equilibrium configuration of the neutral molecule. Doublet states of monocation and singlet states of dication are shown. Green lines correspond to decomposition energies and corresponding transition state energies (TS) for the dication in the ground state. These values are expressed with respect to the ground-state energy of the 1,3-CHD dication [84]. Note that the 1,4-CHD dication ground state is higher in energy than the 1,3-CHD dication ground state, and the former converts into the latter by spontaneous rearrangement. The arrow shows which states are accessible from the ground state of the monocation considering the first electron can acquire a maximum kinetic energy of $3.17U_p$, which corresponds to about 16 eV for a laser intensity of 100 TW/cm^2.

that we measure here. This is consistent with the idea that recollision is expected to play a larger role for molecules since the initial wave function which tunnels into the continuum is larger and therefore spreads less before recolliding, and recollides with a larger target than in the case of an atom.

The correlation plots shown in Fig. 4 indicate that electrons in coincidence with high kinetic-energy release (KER) $C_3H_X{}^+$ and $C_6H_X{}^{2+}$ display similar correlations for the two molecules. In order to compare the two molecules more broadly, we calculated the normalized correlation coefficient for the x component of the electron momenta measured in coincidence with the different fragment ions [59]. Figure 6 shows correlation coefficients for electrons in coincidence with different fragment ions from the two molecules: 1,3-CHD and 1,4-CHD. In order to highlight the importance of the ion kinetic energy filtering to pick out fragments coming from DI, we contrast measurements for electrons in coincidence with high KER fragments (outer ring in the ion momentum distributions) with measurements for electrons in coincidence with low KER fragments (inner ring in the ion momentum distributions). As it can be seen from the plot, electrons in coincidence with low KER ions (inner ring) have correlation coefficient values close to zero (little or no correlation), while electrons in coincidence with high KER ions (outer ring) or the parent dication show significant correlation coefficient values between −0.07 and −0.1.

The lack of correlation for electrons in coincidence with low KER fragment ions stems from the fact that the low KER fragments are due mainly to SI, and the electrons in coincidence with these are mostly false coincidences—i.e., electrons coming from two different molecules in the same laser shot. Thus the correlation values shown here serve as a measure of the correlation that one can expect due to statistics associated with false coincidences. The electrons in coincidence with high KER ions, as well as the parent dication ($C_6H_X{}^{2+}$) show nontrivial correlations compared to electrons in coincidence with low KER ions, which is a good indication of real DI events rather than false coincidences. We also note that the true correlation coefficient for electrons in coincidence with $C_6H_X{}^{2+}$ is likely even more significant than the value shown in the figure, given that $C_6H_X{}^{2+}$ ions are contaminated by low KER $C_3H_X{}^+$ fragments coming from SI.

Figure 6 also compares 1,3-CHD and 1,4-CHD. While only 1,3-CHD is conjugated, and earlier work saw an enhancement of DI in conjugated systems, the two molecules show similar correlation coefficients as well as correlation patterns. It should be pointed out, however, that 1,4-CHD has two double bonds separated by two single bonds, while in previous studies the unconjugated molecules had only single bonds. In order to interpret this point, and our measurements in general, we performed a number of calculations, which are described below.

V. CALCULATION RESULTS

Figure 7 shows the mono- and dicationic energies for both 1,3-CHD and 1,4-CHD obtained from EOM-IP-CCSD calculations. The resulting single and double vertical ionization potential energies from the EOM-IP-CCSD calculations are $I_\mathrm{p}(1) = 8.21$ eV and $I_\mathrm{p}(2) = 22.84$ eV for 1,3-CHD and $I_\mathrm{p}(1) = 8.83$ eV and $I_\mathrm{p}(2) = 23.44$ eV for 1,4-CHD, which are close to the experimental values. The estimated error for the first ionization energy lies under 0.5% (the experimental values are 8.25 eV and 8.82 eV for 1,3-CHD and 1,4-CHD, respectively) and slightly higher (up to 1%) in the case of second ionization energies (experimental value for 1,3-CHD is 22.84 eV) [82]. The calculated lowest electronic transitions in 1,3-CHD$^+$ and 1,4-CHD$^+$ monocations are 2.27 eV and 1.1 eV, respectively (MCQDPT2) or 2.71 and 0.88 eV for EOM-IP-CCSD calculations. When compared to experimental values of 2.58 eV and 1.22 eV [83], the estimated error is 6% for 1,3-CHD and 15% for 1,4-CHD (MCQDPT2). Since we are interested in connecting the molecular structure to the different dissociation channels, the energies of decomposition reactions and corresponding transition states for the dication in singlet states are included. The dissociation energies are taken from Zyubina *et al.* [84] using B3LYP/6-31G** and G3(MP2,CCSD)//B3LYP/6-31G** method. The latter is chemically accurate with estimated errors of 0.9 kcal/mol [85].

The main dissociation products include $C_3H_5{}^+ + C_3H_3{}^+$ [$\Delta E_{\text{diss}} = -1.18$ eV, $\Delta E(\text{TS}) = 2.47$ eV], $C_2H_3{}^+ + C_4H_5{}^+$ [$\Delta E_{\text{diss}} = -0.83$ eV, $\Delta E(\text{TS}) = 2.46$ eV], $C_4H_3{}^+ + C_2H_5{}^+$ [$\Delta E_{\text{diss}} = -1.13$ eV, $\Delta E(\text{TS}) = 2.61$ eV], $C_5H_5{}^+ + CH_3{}^+$ [$\Delta E_{\text{diss}} = -0.15$ eV, $\Delta E(\text{TS}) = 2.49$ eV], $C_6H_7{}^+ + H^+$ [$\Delta E_{\text{diss}} = 1.83$ eV, $\Delta E(\text{TS}) = 3.34$ eV], and $C_6H_6{}^{2+} + H_2$ [$\Delta E_{\text{diss}} = 2.49$ eV, $\Delta E(\text{TS}) = 4.22$ eV]. In contrast to the neutral and monocationic species, the dissociation of dications into two monocations with separation of charge is preferable to the formation of a dication fragment and neutral H atoms. Furthermore, the elimination of a proton is a highly endothermic process, whereas the dissociation to two heavy monocations is exothermic. The barriers to dissociation are indicated in Fig. 7.

Figure 7 highlights the similarities in electronic structure for the two molecules, and the states which are accessible energetically via recollision of the first electron removed by the laser field within one half cycle of the laser. In the simplest approximation (Simpleman's model) [86,87], the energy of the returning electron is determined by the intensity and wavelength or frequency of the driving field, and the phase of the field at which an electron is removed (tunnels into the continuum). The maximum energy of the returning electron is 3.17 times the ponderomotive energy (U_p). This sets a limit on how much energy is available to doubly ionize the molecule via inelastic scattering.

Energies, configurations, and spins resulting from the MCQDPT2 calculations for both molecules are shown in the Appendix (Table I) and energy levels for both 1,3-CHD and 1,4-CHD are displayed in Fig. 8, together with the calculation of the kinetic energy of the electron as a function of the ionization and return times. The MCQDPT2 calculations are qualitatively similar to the EOM-IP-CCSD ones, with the main difference being that MCQDPT2 includes more states at higher energies since it includes double excitations (and singlet and triplet multiplicities). The MCQDPT2 calculations reveal that the ground state of the mono- and dication are doublet and singlet states, respectively, well separated from the excited states, especially for 1,3-CHD, which makes the dynamics for this state quite different. Figure 8 supports the classical estimations that the returning electron has enough energy to excite a second electron to high lying excited states of the monocation (RESI) or to overcome the second ionization potential energy and facilitate RII to the ground state of the dication. In 1,3-CHD only the ground state can be reached, while in 1,4-CHD both the ground and the first excited state are reached within the 3.17 U_p threshold.

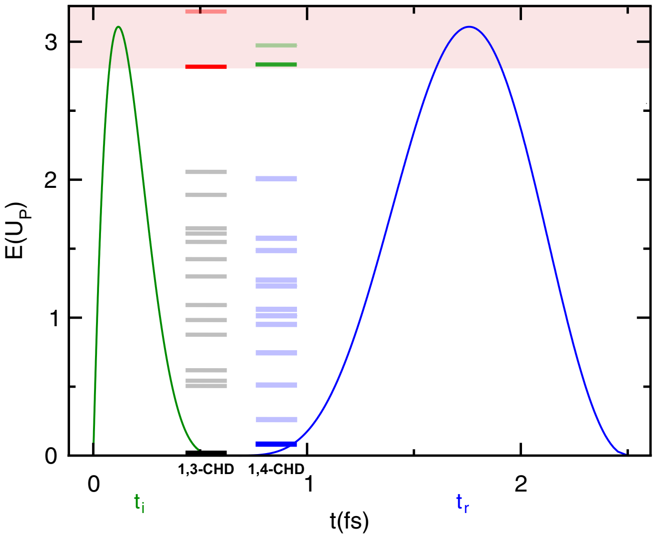

FIG. 8. Relationship between kinetic energy associated with the electron as a function of the ionization time (t_i) and the recollision time (t_r, returning time of first electron to ion core). The energy is shown in units of the ponderomotive energy for an intensity of 100 TW/cm^2. The Simpleman's model has been used here. The mono- and dicationic states calculated by MCQDPT2 are included. Black and red lines correspond to 1,3-CHD mono- and dicationic states, respectively, and blue and green to 1,4-CHD mono- and dicationic states, respectively (ground states are highlighted as thicker lines). The area shaded in red corresponds to energies above the second ionization potential energy. These states are accessible if an electron recollides with a kinetic energy of $3U_p$, allowing the second electron to be excited to high lying states or even directly ionized from the ground state of the monocation. Monocation states at very high energies (above $2U_p$) are not calculated since the active space is limited.

In order to find out if the character of the molecular orbitals can influence the DI dynamics the HOMO, HOMO-1, LUMO, and LUMO + 1 molecular orbitals are plotted in Fig. 9, along with the corresponding Hartree Fock energies. One can observe that the shape of the orbitals does not differ much

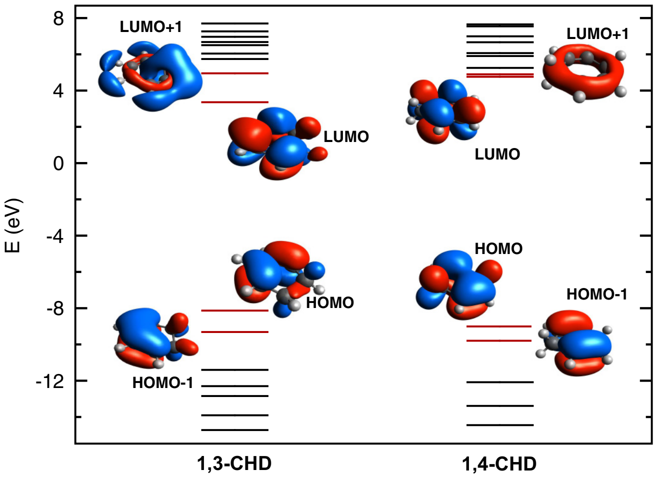

FIG. 9. Relevant molecular orbitals and their energies for 1,3-CHD and 1,4-CHD.

between the two molecules (both molecules involve π orbitals). Since the 1,3-CHD isomer is a conjugated molecule while in 1,4-CHD the double bonds are separated by two single bonds, one would expect the character of the HOMO orbital to be different for the two molecules. In conjugated dienes, the unhybridized *p* orbitals in the carbon atoms overlap to form a π molecular orbital which allows the further delocalization of electrons in the molecule. This delocalization lowers the energy of the system and stabilizes the molecule. For 1,4-CHD, we observe a very similar electronic "cloud" over and under the plane of the molecule, as in 1,3-CHD. This can be explained in terms of hyperconjugation. The interaction of the electrons in a σ orbital (from the C-H bond), with a neighboring unoccupied antibonding π molecular orbital results in an extended molecular orbital. This interaction lowers the energy of the σ occupied orbitals, stabilizing 1,4-CHD. This phenomena can be seen as a perturbation of the π orbitals by the adjacent σ molecular orbitals, which have the same symmetry, changing the energy of these orbitals. The main difference we can observe is the energy difference between HOMO and HOMO-1 orbitals, which for 1,3-CHD is higher than for 1,4-CHD. The ground and excited states in the mono- and dication are closer in energy in 1,4-CHD. Furthermore, the shape of HOMO orbitals in the two molecules is switched. The lowest-energy orbital in 1,3-CHD is the orbital with no nodes in the π system, as expected, while the next orbital (which is the HOMO) has one node. In 1,4-CHD, however, the hyperconjugation lowers the energy of the orbital with one node and makes it the HOMO-1.

VI. DISCUSSION

As discussed in earlier work on DI, the cross pattern in the correlation plots is associated with recollision-induced excitation with subsequent ionization (RESI) [44,49–54]. As Fig. 7 illustrates, for the intensity at which most of our experiments were carried out, the maximum return energy of a rescattering electron (3.17 U_p) is sufficient to excite the molecules to any state of the monocation below the second ionization limit, facilitating RESI. The return energy can also be sufficient to directly remove a second electron, but only from the HOMO or HOMO-1 orbitals, leading to the population of the ground or first excited state of the dication, which is nondissociative. This means that recollision can drive RESI and RII to produce the parent dication, and RESI to produce excited dissociative states of the dication.

RESI and RII have traditionally been considered as different mechanisms, with different signatures in the electron correlation plots. For RESI, the cross pattern arises from the fact that the rescattered electron comes off with high momentum, while the second electron, which is only excited by the rescattering and subsequently ionized in the field, is born near the peak of the field and thus comes off with very low momentum along the laser polarization axis [50,81]. In contrast, RII has been associated with correlated and anticorrelated features—along the diagonal or antidiagonal, depending on the intensity of the field [53,88]. Previous work on N_2 and Ar found that low intensity favored diagonal features in the correlation plots, whereas higher intensities produced antidiagonal features in the correlation plots.

Here, we consider RESI and RII as different limits of inelastic rescattering driven DI, with RII corresponding to the high-energy limit where the returning electron can directly liberate a second weakly bound electron, and RESI corresponding to the low-energy limit, where the rescattering simply leads to excitation of the monocation, followed by field driven removal of the second electron. In between these two limits, there can be variations, including a "high-energy RESI" type rescattering, in which rescattering can lead to the population of high lying states of the monocation, and field assisted removal of a second electron leads to dissociative states of the dication, or a rescattering event that involves a recapture of the first electron to a doubly excited state of the neutral molecule, which can be subsequently ionized by the field. In this case, one might expect to see more anticorrelation due to Coulomb repulsion when both electrons are removed by the field.

As discussed in previous studies [39,89], the intermediate state that the RESI mechanism populates can have a significant impact on the shape of the final momentum correlation. We interpret our DI in terms of this high-energy RESI type mechanism for electrons in coincidence with fragments arising from dissociative DI, and RII plus low-energy RESI for electrons in coincidence with the parent dication. This interpretation is motivated by both the measured correlation plots, which are consistent with the assigned mechanisms, and the calculation results, which indicate that RII can only populate nondissociative states of the dication, and that the majority of excited states of the monocation populated by RESI are correlated with dissociative states of the dication (see Table I in the Appendix).

Previous work on benzene with 30 fs pulses also showed anticorrelation in the correlation plots for electron momenta along the laser polarization, with Coulomb repulsion between the electrons being invoked to explain the anticorrelation [62]. The cross feature was not observed, suggesting that RESI did not play a role at the intensities and for the longer pulse durations used in that work. Earlier work on Ar atoms also found a cross pattern associated with RESI in the limit of short pulses (<10 fs), but not for longer pulses (10–30 fs) [53].

In order to evaluate the significance of rescattering driven ionization, we consider the probability for inelastic scattering. Previous work on atoms [90] and molecules [91] shows that inelastic scattering cross sections can be comparable to or larger than elastic scattering cross sections for the return energies present at our laser intensities, with probabilities on the order of a few percent. A simple calculation supports this notion. A free electron wave packet with an initial width of 8 a.u. ($\sim$4 Å) will expand to 9.43 a.u. ($\sim$4.7 Å) in about 80 a.u. ($\sim$2 fs), leading to a a cross-sectional area of $\sim$0.22 nm^2 (22×10^{-16} cm^2). For an inelastic electron impact excitation cross section of 10^{-16} cm^2, the excitation probability is then roughly 4%. While such an estimation is quite coarse, it is consistent with recent measurements and calculations of rescattering in butadiene [91], suggesting that the calculation provides an accurate order of magnitude estimate. The calculation underscores the point that rescattering can play a much more important role in molecular DI than atomic DI (for molecules composed of comparable atoms) because the size of the molecule leads to a larger initial electron wave function

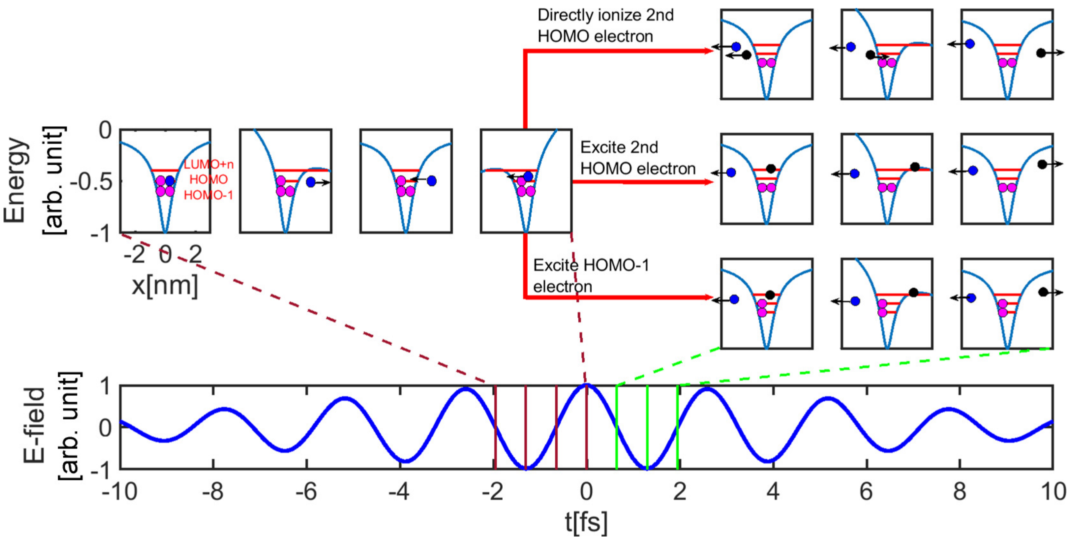

FIG. 10. Illustration of the RESI and RII dynamics. This figure shows the time-dependent laser field (lower panel) as well as the most loosely bound electrons in a model potential (upper panel). The energy plots are separated into three pathways upon rescattering. The upper panel shows nondissociative channels where both HOMO electrons are removed via RII, with Coulomb repulsion between the two electrons. The middle panel shows a nondissociative channel driven by RESI. The bottom panel shows a dissociative channel where at least one electron is removed from deeper-bound HOMO-n (here only shows $n = 1$) orbital due to RESI. The brown vertical lines mark laser times corresponding to tunnel ionization, acceleration in the field, and the return of the first electron, while green vertical lines mark events during the rescattering dynamics.

in the target, which spreads less during the time between ionization and recollision, and also finds a much larger target on coming back to the molecule as compared with an atom. We note that high Z atoms can also have larger DI:SI ratios compared with low Z atoms [23].

Figure 10 illustrates both RESI and RII, with the possibility of recollisional excitation of more deeply bound orbitals highlighted. Given the pulse duration of about 10 fs, the optical period of 2.6 fs, and the nonlinear dependence of tunnel ionization on field strength, ionzation is confined to a few cycles near the peak of the pulse, which does not leave time for many recollisions, and means that the probability for two electrons to leave the molecule during the same field cycle is higher than for a longer pulse. It does not leave time for nuclear dynamics either, since the pulse duration is shorter than the fastest vibrational period in the molecule [92]. These considerations motivate the focus on the subcycle ionization and recollision dynamics taking place.

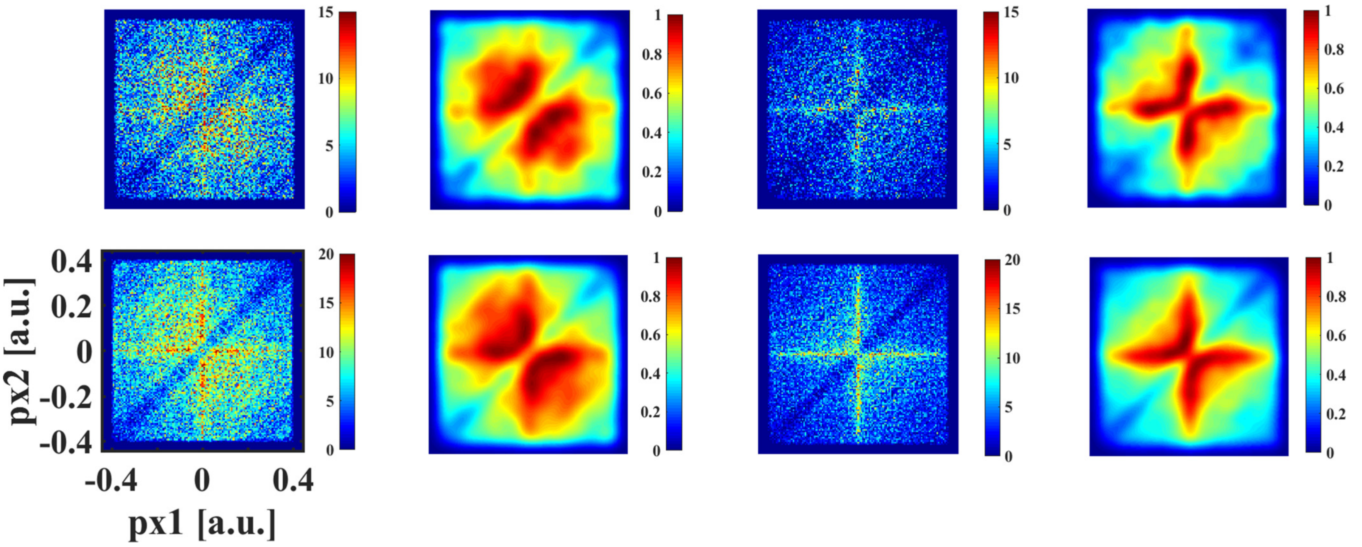

FIG. 11. Comparison of correlation plots with and without smoothing. The smoothed plots are the same as shown in Fig. 4, and the plots to their left show the same results without smoothing. The two panels on the top left correspond to nondissociative DI of 1,3-CHD. The two panels on the bottom left correspond to nondissociative DI of 1,4-CHD. The two panels on the top right correspond to dissociative DI of 1,3-CHD. The two panels on the bottom right correspond to dissociative DI of 1,4-CHD.

VII. CONCLUSION

In conclusion, we have observed differences in the correlations between electrons emitted along the laser polarization in molecular DI, with electrons coming from dissociative DI behaving differently than electrons coming from nondissociative DI. Measurements for two similar molecules show similar behavior. We interpret our measurements with the help of electronic structure calculations and determine that different mechanisms dominate for the two different channels. Our measurements and interpretation illustrate the importance of rescattering in strong-field molecular ionization, and highlight the richness of the rescattering dynamics.

ACKNOWLEDGMENTS

The authors would like to acknowledge very helpful and informative discussions with Jan Chaloupka and Daniel Rolles as well as technical assistance from Brian M. Kaufman and Anbu Venkatachalam. We gratefully acknowledge support from the Department of Energy under Awards No. DE-FG02-08ER15984 and No. DE-FG02-08ER15983.

APPENDIX

The correlation plots shown in the main body of the manuscript were smoothed in order to focus the reader's attention on the main features. However, in order to see finer features and get a better sense of the statistical significance of the features, we provide a comparison here of the smoothed versus unsmoothed correlation plots, which is shown in Fig. 11. And we compare the similarities between quadruple (2*i*2*e*) and triple (1*i*2*e*) coincidence events in order to show the validity of looking at 1*i*2*e* events. In Fig. 12, we compare the two methods for the channel resulting in a $C_1H_X{}^+$ and $C_5H_X{}^+$ ion pair. The upper panel shows the correlation plot for 2*i*2*e* events in coincidence with $C_1H_X{}^+$ and $C_5H_X{}^+$ ions. The bottom left and right panels are correlation plots for electrons in coincidence with $C_1H_X{}^+$ and $C_5H_X{}^+$ ions, respectively. The contributions of false coincidences have been suppressed by lowering the electron detection rate to lower than 0.4 per shot. In order to select 1*i*2*e* events for which both electrons come from DI, we only consider events where the ion KER is above 0.5 eV. From the three plots, we can see that 2*i*2*e* events show the same features as $C_1H_X{}^+$ or $C_5H_X{}^+$ 1*i*2*e* events. The small differences between the 1*i*2*e* and 2*i*2*e* correlation plots are a result of limited statistics and false coincidences.

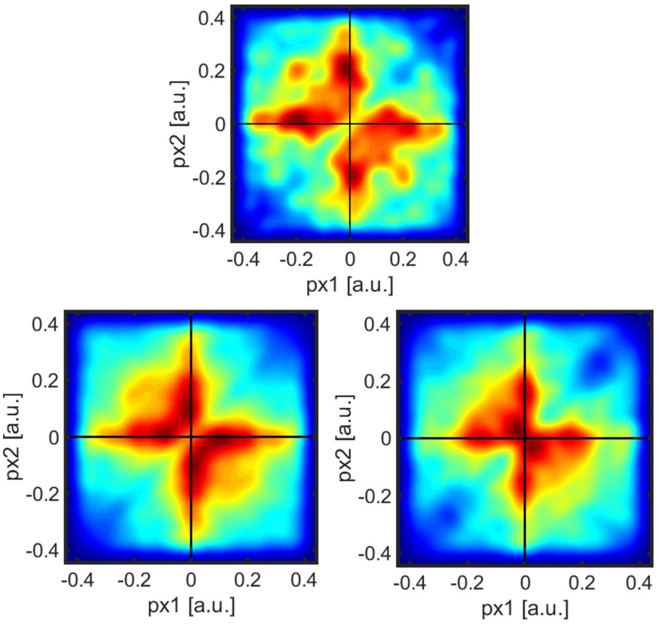

FIG. 12. Comparison of correlation plots for a specific DI channel of 1,3-CHD. The measurements were performed for a peak intensity of 100 TW/cm^2. The upper panel corresponds to electrons from 2*i*2*e* events producing $C_1H_X{}^+$ and $C_5H_X{}^+$. The lower panels are for electrons from 1*i*2*e* events with $C_1H_X{}^+$ and $C_5H_X{}^+$, respectively.

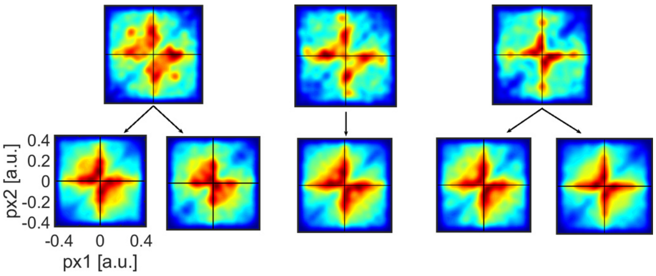

FIG. 13. Full comparison of correlation plots for 1*i*2*e* and 2*i*2*e* measurements of different dissociative DI channels of 1,3-CHD. The experimental data was taken with a peak intensity of 100 TW/cm^2. The upper panels are the three correlation plots for 2*i*2*e* events (from left to right: $C_1H_X{}^+$ and $C_5H_X{}^+$; $C_3H_X{}^+$ and $C_3H_X{}^+$; $C_2H_X{}^+$ and $C_4H_X{}^+$). The lower panels are the five correlation plots for all different 1*i*2*e* coincidences (from left to right: $C_1H_X{}^+$; $C_5H_X{}^+$; $C_3H_X{}^+$; $C_2H_X{}^+$; $C_4H_X{}^+$).

We also provide a full comparison of all quadruple and triple coincidence measurements for all dissociative DI channels. The upper panels of Fig. 13 show the correlation plots for quadruple coincidence measurements (2*i*2*e*) of the three main dissociative channels: $C_1H_X{}^+$ and $C_5H_X{}^+$, $C_3H_X{}^+$ and $C_3H_X{}^+$, and $C_2H_X{}^+$ and $C_4H_X{}^+$, respectively. The lower panels show the correlation plots for triple coincidence measurements (1*i*2*e*) of the same dissociation products: $C_nH_X{}^+$, where $n = 1, \dots, 5$. This comparison shows that the 2*i*2*e* and 1*i*2*e* events provide similar information on the electron correlation. Furthermore, it highlights the fact that different 2*i*2*e* or 1*i*2*e* events for these dissociative channels show consistent features as reported in the main text.

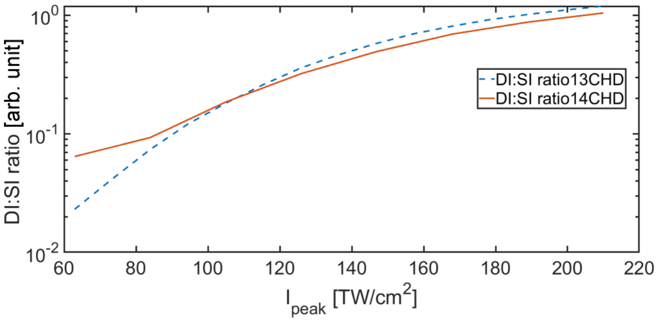

FIG. 14. Noncoincidence intensity scan of DI to SI ratio for 1,3-CHD and 1,4-CHD.

TABLE I. Table of mono- and dicationic energy levels, configurations, and spins ("S" for singlet and "T" for triplet) of 1,3-CHD and 1,4-CHD calculated at the MCQDPT2 level. When no spin is indicated all states are doublets (in monocations). The electrons and orbitals in the active space are shown. The active space for monocations has 17 electrons in 13 orbitals, while in dications it has 16 electrons in 11 orbitals. More virtual orbitals are included in monocations in order to be able to describe more states.

CHD$^+$				CHD^{2+}					
1,3-CHD		1,4-CHD		1,3-CHD			1,4-CHD		
Conf	Energy (eV)	Conf	Energy (eV)	Conf	Energy (eV)	Spin	Conf	Energy (eV)	Spin
22222222+0000	0	22222222+0000	0.48	22222222000	0	S	22222222000	0.47	S
2222222+20000	2.43	2222222+20000	1.51	2222222++00	1.72	T	2222222++00	0.86	T
222222+220000	2.66	222222+220000	2.58	222222+2+00	1.92	T	222222+2+00	1.91	T
22222+2220000	2.91	22222+2220000	3.66	2222222+2−00	2.23	S	222222+2−00	2.29	S
222222220+000	3.97	2222+22220000	4.69	22222+22+00	2.39	T	2222222+−00	2.65	S
2222+22220000	4.28	222222220+000	5.06	22222+22−00	2.74	S	222222++200	3.18	T
22+2222220000	4.68	2+22222220000	5.32	2222+222+00	3.17	T	22222+22+00	3.34	T
222+222220000	4.87	222+222220000	5.49	2222222+−00	3.19	S	222222+−200	3.50	S
+222222220000	5.66	2222222200+00	5.73	2222+222−00	3.62	S	22222220200	3.78	S
2222222200+00	5.98	+222222220000	6.12	222+2222+00	3.84	T	22222+22−00	3.88	S
2+22222220000	6.53	22+2222220000	6.33	222+2222−00	4.10	S	222+2222+00	4.27	T

The DI to SI ratio as a function of intensity for both 1,3-CHD and 1,4-CHD is shown in Fig. 14. Our measured ratios are much larger than those measured for atoms [81].

Table I provides the energies and configurations of electronic states for the mono- and dications of both 1,3-CHD and 1,4-CHD. Most excited states of the monocation have configurations with holes in orbitals below the HOMO.

---

[1] M. F. Kling and M. J. Vrakking, Annu. Rev. Phys. Chem. **59**, 463 (2008).

[2] F. Krausz and M. Ivanov, Rev. Mod. Phys. **81**, 163 (2009).

[3] M. Nisoli, P. Decleva, F. Calegari, A. Palacios, and F. Martín, Chem. Rev. **117**, 10760 (2017).

[4] P. B. Corkum, Phys. Rev. Lett. **71**, 1994 (1993).

[5] J. L. Krause, K. J. Schafer, and K. C. Kulander, Phys. Rev. A **45**, 4998 (1992).

[6] P. Agostini and L. F. DiMauro, Contemp. Phys. **49**, 179 (2008).

[7] M. Lewenstein, P. Balcou, M. Y. Ivanov, A. L'Huillier, and P. B. Corkum, Phys. Rev. A **49**, 2117 (1994).

[8] A. McPherson, G. Gibson, H. Jara, U. Johann, T. S. Luk, I. A. McIntyre, K. Boyer, and C. K. Rhodes, J. Opt. Soc. Am. B **4**, 595 (1987).

[9] T. Zuo, A. Bandrauk, and P. Corkum, Chem. Phys. Lett. **259**, 313 (1996).

[10] M. Meckel, D. Comtois, D. Zeidler, A. Staudte, D. Pavičić, H. C. Bandulet, H. Pépin, J. C. Kieffer, R. Dörner, D. M. Villeneuve, and P. B. Corkum, Science **320**, 1478 (2008).

[11] C. I. Blaga, J. Xu, A. D. DiChiara, E. Sistrunk, K. Zhang, P. Agostini, T. A. Miller, L. F. DiMauro, and C. Lin, Nature (London) **483**, 194 (2012).

[12] Z. Vager, R. Naaman, and E. Kanter, Science **244**, 426 (1989).

[13] F. Légaré, K. F. Lee, I. V. Litvinyuk, P. W. Dooley, S. S. Wesolowski, P. R. Bunker, P. Dombi, F. Krausz, A. D. Bandrauk, D. M. Villeneuve, and P. B. Corkum, Phys. Rev. A **71**, 013415 (2005).

[14] H. Stapelfeldt, E. Constant, H. Sakai, and P. B. Corkum, Phys. Rev. A **58**, 426 (1998).

[15] B. Feuerstein, T. Ergler, A. Rudenko, K. Zrost, C. D. Schröter, R. Moshammer, J. Ullrich, T. Niederhausen, and U. Thumm, Phys. Rev. Lett. **99**, 153002 (2007).

[16] W. Becker, X. J. Liu, P. J. Ho, and J. H. Eberly, Rev. Mod. Phys. **84**, 1011 (2012).

[17] A. l'Huillier, L. A. Lompre, G. Mainfray, and C. Manus, Phys. Rev. A **27**, 2503 (1983).

[18] L. F. DiMauro, D. Kim, M. W. Courtney, and M. Anselment, Phys. Rev. A **38**, 2338 (1988).

[19] D. N. Fittinghoff, P. R. Bolton, B. Chang, and K. C. Kulander, Phys. Rev. Lett. **69**, 2642 (1992).

[20] B. Walker, B. Sheehy, L. F. DiMauro, P. Agostini, K. J. Schafer, and K. C. Kulander, Phys. Rev. Lett. **73**, 1227 (1994).

[21] K. Kondo, A. Sagisaka, T. Tamida, Y. Nabekawa, and S. Watanabe, Phys. Rev. A **48**, R2531 (1993).

[22] S. Larochelle, A. Talebpour, and S. L. Chin, J. Phys. B: At., Mol., Opt. Phys. **31**, 1201 (1998).

[23] J. L. Chaloupka, J. Rudati, R. Lafon, P. Agostini, K. C. Kulander, and L. F. DiMauro, Phys. Rev. Lett. **90**, 033002 (2003).

[24] A. Talebpour, S. Larochelle, and S. L. Chin, J. Phys. B: At., Mol., Opt. Phys. **30**, L245 (1997).

[25] C. Cornaggia and P. Hering, J. Phys. B: At., Mol., Opt. Phys. **31**, L503 (1998).

[26] C. Guo, M. Li, J. P. Nibarger, and G. N. Gibson, Phys. Rev. A **61**, 033413 (2000).

[27] C. Cornaggia and P. Hering, Phys. Rev. A **62**, 023403 (2000).

[28] A. Becker and F. H. M. Faisal, Phys. Rev. Lett. **89**, 193003 (2002).

[29] U. Eichmann, M. Dörr, M. Maeda, W. Becker, and W. Sandner, Phys. Rev. Lett. **84**, 3550 (2000).

[30] R. Moshammer, B. Feuerstein, W. Schmitt, A. Dorn, C. D. Schröter, J. Ullrich, H. Rottke, C. Trump, M. Wittmann, G. Korn, K. Hoffmann, and W. Sandner, Phys. Rev. Lett. **84**, 447 (2000).

[31] K. C. Kulander, J. Cooper, and K. J. Schafer, Phys. Rev. A **51**, 561 (1995).

[32] A. Becker and F. H. M. Faisal, Phys. Rev. Lett. **84**, 3546 (2000).

[33] S. P. Goreslavskii, S. V. Popruzhenko, R. Kopold, and W. Becker, Phys. Rev. A **64**, 053402 (2001).

[34] C. Figueira de Morisson Faria, H. Schomerus, X. Liu, and W. Becker, Phys. Rev. A **69**, 043405 (2004).

[35] J. S. Parker, B. J. S. Doherty, K. T. Taylor, K. D. Schultz, C. I. Blaga, and L. F. DiMauro, Phys. Rev. Lett. **96**, 133001 (2006).

[36] M. Lein, E. K. U. Gross, and V. Engel, J. Phys. B: At., Mol., Opt. Phys. **33**, 433 (2000).

[37] A. Staudte, C. Ruiz, M. Schöffler, S. Schössler, D. Zeidler, T. Weber, M. Meckel, D. M. Villeneuve, P. B. Corkum, A. Becker, and R. Dörner, Phys. Rev. Lett. **99**, 263002 (2007).

[38] D. I. Bondar, W.-K. Liu, and M. Y. Ivanov, Phys. Rev. A **79**, 023417 (2009).

[39] E. Eremina, X. Liu, H. Rottke, W. Sandner, M. G. Schätzel, A. Dreischuh, G. G. Paulus, H. Walther, R. Moshammer, and J. Ullrich, Phys. Rev. Lett. **92**, 173001 (2004).

[40] Y. Liu, S. Tschuch, A. Rudenko, M. Dürr, M. Siegel, U. Morgner, R. Moshammer, and J. Ullrich, Phys. Rev. Lett. **101**, 053001 (2008).

[41] E. Eremina, X. Liu, H. Rottke, W. Sandner, A. Dreischuh, F. Lindner, F. Grasbon, G. G. Paulus, H. Walther, R. Moshammer, B. Feuerstein, and J. Ullrich, J. Phys. B: At., Mol., Opt. Phys. **36**, 3269 (2003).

[42] B. Feuerstein, R. Moshammer, D. Fischer, A. Dorn, C. D. Schröter, J. Deipenwisch, J. R. Crespo Lopez-Urrutia, C. Höhr, P. Neumayer, J. Ullrich, H. Rottke, C. Trump, M. Wittmann, G. Korn, and W. Sandner, Phys. Rev. Lett. **87**, 043003 (2001).

[43] D. Zeidler, A. Staudte, A. B. Bardon, D. M. Villeneuve, R. Dörner, and P. B. Corkum, Phys. Rev. Lett. **95**, 203003 (2005).

[44] T. Shaaran, M. T. Nygren, and C. Figueira de Morisson Faria, Phys. Rev. A **81**, 063413 (2010).

[45] V. L. B. de Jesus, B. Feuerstein, K. Zrost, D. Fischer, A. Rudenko, F. Afaneh, C. D. Schröter, R. Moshammer, and J. Ullrich, J. Phys. B: At., Mol., Opt. Phys. **37**, L161 (2004).

[46] N. Camus, B. Fischer, M. Kremer, V. Sharma, A. Rudenko, B. Bergues, M. Kübel, N. G. Johnson, M. F. Kling, T. Pfeifer, J. Ullrich, and R. Moshammer, Phys. Rev. Lett. **108**, 073003 (2012).

[47] C. Huang, W. Guo, Y. Zhou, and Z. Wu, Phys. Rev. A **93**, 013416 (2016).

[48] B. Eckhardt, J. S. Prauzner-Bechcicki, K. Sacha, and J. Zakrzewski, Chem. Phys. **370**, 168 (2010).

[49] B. Bergues, M. Kübel, N. G. Kling, C. Burger, and M. F. Kling, IEEE J. Sel. Top. Quantum Electron. **21**, 1 (2015).

[50] Y.-B. Li, X. Wang, B.-H. Yu, Q.-B. Tang, G.-H. Wang, and J.-G. Wan, Sci. Rep. **6**, 37413 (2016).

[51] B. Bergues, M. Kübel, N. G. Johnson, B. Fischer, N. Camus, K. J. Betsch, O. Herrwerth, A. Senftleben, A. M. Sayler, T. Rathje, T. Pfeifer, I. Ben-Itzhak, R. R. Jones, G. G. Paulus, F. Krausz, R. Moshammer, J. Ullrich, and M. F. Kling, Nat. Commun. **3**, 813 (2012).

[52] M. Kübel, N. G. Kling, K. J. Betsch, N. Camus, A. Kaldun, U. Kleineberg, I. Ben-Itzhak, R. R. Jones, G. G. Paulus, T. Pfeifer *et al.*, Phys. Rev. A **88**, 023418 (2013).

[53] M. Kübel, K. Betsch, N. G. Kling, A. Alnaser, J. Schmidt, U. Kleineberg, Y. Deng, I. Ben-Itzhak, G. Paulus, T. Pfeifer *et al.*, New J. Phys. **16**, 033008 (2014).

[54] T. Shaaran, C. Figueira de Morisson Faria, and H. Schomerus, Phys. Rev. A **85**, 023423 (2012).

[55] Q. Li, Y. Zhou, and P. Lu, J. Phys. B: At., Mol., Opt. Phys. **50**, 225601 (2017).

[56] X. Y. Jia, W. D. Li, J. Fan, J. Liu, and J. Chen, Phys. Rev. A **77**, 063407 (2008).

[57] C. Figueira de Morisson Faria, T. Shaaran, X. Liu, and W. Yang, Phys. Rev. A **78**, 043407 (2008).

[58] A. Zhao, P. Sándor, V. Tagliamonti, S. Matsika, and T. Weinacht, J. Phys. Chem. A **120**, 3233 (2016).

[59] A. Zhao, C. Cheng, S. Matsika, and T. Weinacht, Phys. Rev. A **97**, 043412 (2018).

[60] X. Gong, Q. Song, Q. Ji, K. Lin, H. Pan, J. Ding, H. Zeng, and J. Wu, Phys. Rev. Lett. **114**, 163001 (2015).

[61] K. Lin, X. Jia, Z. Yu, F. He, J. Ma, H. Li, X. Gong, Q. Song, Q. Ji, W. Zhang, H. Li, P. Lu, H. Zeng, J. Chen, and J. Wu, Phys. Rev. Lett. **119**, 203202 (2017).

[62] A. H. Winney, Y. F. Lin, S. K. Lee, P. Adhikari, and W. Li, Phys. Rev. A **93**, 031402(R) (2016).

[63] M. Dugan, J. Tull, and W. Warren, J. Opt. Soc. Am. B **14**, 2348 (1997).

[64] M. R. Fetterman, D. Goswami, D. Keusters, W. Yang, J.-K. Rhee, and W. S. Warren, Opt. Express **3**, 366 (1998).

[65] M. Fisher-Levine and A. Nomerotski, J. Instrum. **11**, C03016 (2016).

[66] A. Nomerotski, I. Chakaberia, M. Fisher-Levine, Z. Janoska, P. Takacs, and T. Tsang, J. Instrum. **12**, C01017 (2017).

[67] J. Ullrich, R. Moshammer, A. Dorn, R. Dörner, L. P. H. Schmidt, and H. Schmidt-Böcking, Rep. Prog. Phys. **66**, 1463 (2003).

[68] A. D. Becke, J. Chem. Phys. **98**, 5648 (1993).

[69] C. Lee, W. Yang, and R. G. Parr, Phys. Rev. B **37**, 785 (1988).

[70] Gaussian 09, Revision E.01, M. J. Frisch, G. W. Trucks, H. B. Schlegel, G. E. Scuseria, M. A. Robb, J. R. Cheeseman, G. Scalmani, V. Barone, B. Mennucci, G. A. Petersson, H. Nakatsuji, M. Caricato, X. Li, H. P. Hratchian, A. F. Izmaylov, J. Bloino, G. Zheng, J. L. Sonnenberg, M. Hada, M. Ehara, K. Toyota, R. Fukuda, J. Hasegawa, M. Ishida, T. Nakajima, Y. Honda, O. Kitao, H. Nakai, T. Vreven, J. A. Montgomery, Jr., J. E. Peralta, F. Ogliaro, M. Bearpark, J. J. Heyd, E. Brothers, K. N. Kudin, V. N. Staroverov, R. Kobayashi, J. Normand, K. Raghavachari, A. Rendell, J. C. Burant, S. S. Iyengar, J. Tomasi, M. Cossi, N. Rega, J. M. Millam, M. Klene, J. E. Knox, J. B. Cross, V. Bakken, C. Adamo, J. Jaramillo, R. Gomperts, R. E. Stratmann, O. Yazyev, A. J. Austin, R. Cammi, C. Pomelli, J. W. Ochterski, R. L. Martin, K. Morokuma, V. G. Zakrzewski, G. A. Voth, P. Salvador, J. J. Dannenberg, S. Dapprich, A. D. Daniels, Ö. Farkas, J. B. Foresman, J. V. Ortiz, J. Cioslowski, and D. J. Fox (Gaussian, Inc., Wallingford, CT, 2009).

[71] J. F. Stanton and R. J. Bartlett, J. Chem. Phys. **98**, 7029 (1993).

[72] M. Head-Gordon, R. J. Rico, M. Oumi, and T. J. Lee, Chem. Phys. Lett. **219**, 21 (1994).

[73] A. I. Krylov, Annu. Rev. Phys. Chem. **59**, 433 (2008).

[74] Y. Shao, Z. Gan, E. Epifanovsky, A. T. B. Gilbert, M. Wormit, J. Kussmann, A. W. Lange, A. Behn, J. Deng, X. Feng, D. Ghosh, M. Goldey, P. R. Horn, L. D. Jacobson, I. Kaliman *et al.*, Mol. Phys. **113**, 184 (2015).

[75] H. Nakano, J. Chem. Phys. **99**, 7983 (1993).

[76] H. Nakano, Chem. Phys. Lett. **207**, 372 (1993).

[77] M. W. Schmid, K. K. Baldridge, J. A. Boatz, S. T. Elbert, M. S. Gordon, J. H. Jensen, S. Koseki, N. Matsunaga, K. A. Nguyen, S. Su, T. L. Windus, M. Dupuis, and J. A. Montgomery, Jr., J. Comput. Chem. **14**, 1347 (1993).

[78] M. S. Gordon and M. W. Schmidt, in *Theory and Applications of Computational Chemistry*, edited by C. E. Dykstra, G. Frenking, K. S. Kim, and G. E. Scuseria (Elselvier, Amsterdam, 2005), pp. 1167–1189.

[79] T. H. Dunning, J. Chem. Phys. **90**, 1007 (1989).

[80] X.-M. Tong, Z. X. Zhao, and C.-D. Lin, Phys. Rev. A **66**, 033402 (2002).

[81] M. Kübel, C. Burger, N. G. Kling, T. Pischke, L. Beaufore, I. Ben-Itzhak, G. G. Paulus, J. Ullrich, T. Pfeifer, R. Moshammer *et al.*, Phys. Rev. A **93**, 053422 (2016).

[82] H. Harada, S. Shimizu, T. Yatsuhashi, S. Sakabe, Y. Izawa, and N. Nakashima, Chem. Phys. Lett. **342**, 563 (2001).

[83] T. Shida, *Electronic Absorption Spectra of Radical Ions* (Elsevier Science Ltd., Amsterdam, 1988), Vol. 34.

[84] T. S. Zyubina, A. M. Mebel, M. Hayashi, and S. H. Lin, Phys. Chem. Chem. Phys. **10**, 2321 (2008).

[85] C. J. Cramer, *Essentials of Computational Chemistry: Theories and Models* (John Wiley & Sons, Chichester, England, 2004), 2nd ed.

[86] J. L. Krause, K. J. Schafer, and K. C. Kulander, Phys. Rev. Lett. **68**, 3535 (1992).

[87] G. G. Paulus, W. Becker, W. Nicklich, and H. Walther, J. Phys. B: At., Mol., Opt. Phys. **27**, L703 (1994).

[88] A. Emmanouilidou and A. Staudte, Phys. Rev. A **80**, 053415 (2009).

[89] T. Shaaran, B. B. Augstein, and C. Figueira de Morisson Faria, Phys. Rev. A **84**, 013429 (2011).

[90] O. Zatsarinny, H. Parker, and K. Bartschat, Phys. Rev. A **99**, 012706 (2019).

[91] F. Schell, T. Bredtmann, C. P. Schulz, S. Patchkovskii, M. J. Vrakking, and J. Mikosch, Sci. Adv. **4**, 8148 (2018).

[92] P. Sándor, V. Tagliamonti, A. Zhao, T. Rozgonyi, M. Ruckenbauer, P. Marquetand, and T. Weinacht, Phys. Rev. Lett. **116**, 063002 (2016).